

Instabilities of Spiral Shocks I: Onset of Wiggle Instability and its Mechanism

Keiichi Wada,¹* and Jin Koda,^{1,2†}

¹ National Astronomical Observatory of Japan, Mitaka, Tokyo 181-8588, Japan

² Department of Astronomy, California Institute of Technology, MS 105-24, Pasadena, CA 91125, USA

Accepted Dec. 2, 2003, Received ; in original form

ABSTRACT

We found that loosely wound spiral shocks in an isothermal gas disk caused by a non-axisymmetric potential are hydrodynamically unstable, if the shocks are strong enough. High resolution, global hydrodynamical simulations using three different numerical schemes, i.e. AUSM, CIP, and SPH, show similarly that trailing spiral shocks with the pitch angle of larger than $\sim 10^\circ$ wiggle, and clumps are developed in the shock-compressed layer. The numerical simulations also show clear wave crests that are associated with ripples of the spiral shocks. The spiral shocks tend to be more unstable in a rigidly rotating disk than in a flat rotation. This instability could be an origin of the secondary structures of spiral arms, i.e. the spurs/fin, observed in spiral galaxies. In spite of this local instability, the global spiral morphology of the gas is maintained over many rotational periods. The Kelvin-Helmholtz (K-H) instability in a shear layer behind the shock is a possible mechanism for the wiggle instability. The Richardson criterion for the K-H stability is expressed as a function of the Mach number, the pitch angle, and strength of the background spiral potential. The criterion suggests that spiral shocks with smaller pitch angles and smaller Mach numbers would be more stable, and this is consistent with the numerical results.

Key words: hydrodynamics – instability – galaxies: spiral

1 INTRODUCTION

Spiral arms are the most prominent substructure in disc galaxies. The spiral density wave hypothesis (Lin & Shu 1964) has been widely accepted as explaining the steady stellar spiral structure. The spiral density waves cause shocks in the interstellar medium, i.e. the galactic shocks. This phenomenon was well studied in the 60s and 70s. Compression of the interstellar medium behind the shocks is an essential mechanism in the formation of massive stars that illuminate the spiral structure. Assuming tightly wound spirals and steady flow, linear and weak nonlinear response of the gas in the spiral potential has been studied. (Fujimoto 1968; Roberts 1969; Shu et al. 1972; Shu, Milione, & Roberts 1973).

Most of these initial studies adopted rather simple assumptions for the ISM, i.e. isothermal equation of state and single-phase, uniform and non-selfgravitating gas. Then, more realistic cases were studied. For example, Sawa (1977) investigated effects of the selfgravity of the gas on the asymptotic stationary solution. Ishibashi & Yoshii (1984)

studied an energy loss flow. Tomisaka (1987) took into account the thermal heating and cooling processes for the cloud fluid. Lubow, Cowie, & Balbus (1986) studied two-component flow, i.e. isothermal gas and stars. Among these studies, the spiral potential was assumed to be tightly wound, and a periodic boundary condition was applied. These studies focused on the steady state of the gas in a spiral potential, because the observed spirals are thought to be a long-lived structure in galaxies. Woodward (1975), on the other hand, studied gas flow in a tightly wound spiral potential, using time-dependent numerical simulations under the same approximation adopted by Roberts (1969), and showed that shocks are formed within one or two transits of the gas through the spiral pattern. Johns & Nelson (1986) performed numerical simulations on a time-dependent, two-dimensional gaseous response in a spiral potential, and found that quasi-steady spiral shocks are formed.

The next question concerns the stability of the galactic shock: Nelson & Matsuda (1977) showed that tightly wound spiral shocks are dynamically stable. Dwarkadas & Balbus (1996) discussed the linear stability of the spiral shocks assuming a flat rotation curve and concluded that the flow is stable. Mishurov & Suchkov (1975) showed that the flow obtained by Roberts (1969) turns out to be stable behind

* E-mail: wada.keiichi@nao.ac.jp

† JSPS fellow, E-mail: koda@astro.caltech.edu

the shock front. On the other hand, it is unstable ahead of the shock. Recently, Kim & Ostriker (2002) performed two-dimensional, shearing box simulations of the magnetized gas in a spiral potential in an effort to understand the origin of the secondary structure in spiral arms, namely ‘spurs’ (Elmegreen 1980). They found that gaseous spurs are formed as a consequence of magneto-gravitational instabilities inside spiral arms (see also Balbus (1988) for the linear analysis). Gravitational stability of the shocked gas in spiral arms has been well studied in the context of the formation of the giant molecular clouds (e.g. Elmegreen 1994).

In most of the studies mentioned above, spiral shocks are assumed to be tightly wound, i.e. their pitch angles are smaller than 10° , and a flat rotation curve which is in general suitable for the galactic outer disk is also assumed. In this paper, we investigate stability of the gas flow in more general spiral potentials, with small ($\sim 5^\circ$) to large ($\sim 20^\circ$) pitch angles in various rotation curves. We perform two-dimensional, time-dependent, global hydrodynamical simulations of the gas in spiral and barred potentials using three high-resolution numerical schemes based on different concepts. We show that the spiral shocks generated in a *non-self-gravitating* thin disc may be dynamically *unstable*, in the sense that the shock front *wiggles*, and eventually knots are formed in the shock-compressed gas (section 2 and section 3). The physical origin of this instability in terms of the Kelvin-Helmholtz (K-H) instability in a shocked layer, as well as other implication from the numerical results will be discussed in section 4. A brief summary and conclusions are given in section 5. In Appendix, the Richardson criterion behind the spiral shock is approximately derived.

Non-linear and long-term evolution of the instability and comparison with observations, such as spurs/fins in galaxies, and dynamics of the multi-phase, self-gravitating interstellar medium in the spiral potential will be discussed in subsequent papers.

2 NUMERICAL SIMULATIONS

2.1 Methods

As we will see in section 3, hydrodynamical simulations show that the spiral shocked layer is unstable in some situations. In order to ensure that the instabilities are not caused by numerical artifacts, we apply three hydrodynamical schemes based on different physical and numerical concepts to the same models, i.e. an Euler mesh code (AUSM: Advection Upstream Splitting Method), mesh-based semi-Lagrangian code (CIP: Cubic-polynomial Interpolation), and particle-based Lagrangian code (SPH: Smoothed Particle Hydrodynamics). We find that the instability commonly occurs among results with these three codes. All these schemes are standard methods in computational fluid dynamics and astrophysical gas dynamics. We briefly describe the three numerical schemes below:

2.1.1 AUSM

AUSM was developed by Liou & Steffen (1993), and has been widely used for aerodynamical simulations. AUSM is remarkably simple, but it is accurate enough based on a

comparison with Flux-difference splitting schemes (e.g. Roe splitting) and PPM (?). The two-dimensional and three-dimensional versions of the scheme with a Poisson equation solver were applied to various problems of dynamics of the interstellar medium (Wada 2001; Wada & Norman 1999, 2001, 2002; Wada, Spaans, & Kim 2001; Wada, Gerhardt, & Norman 2002). We summarize the essential points of AUSM below.

The basic equations for the isothermal two-dimensional flow are written as

$$\frac{\partial \mathbf{U}}{\partial t} + \frac{\partial \mathbf{F}}{\partial x} + \frac{\partial \mathbf{G}}{\partial y} = 0, \quad (1)$$

where $\mathbf{U}^T \equiv (\rho, \rho u, \rho v)$, $\mathbf{F}^T \equiv [\rho u, \rho u^2 + p, \rho uv]$, $\mathbf{G}^T \equiv [\rho v, \rho vu, \rho v^2 + p]$.

Flux \mathbf{F} and \mathbf{G} consist of two physically distinct parts, namely advection and pressure terms:

$$\mathbf{F} = \begin{pmatrix} \rho \\ \rho u \\ \rho v \end{pmatrix} u + \begin{pmatrix} 0 \\ p \\ 0 \end{pmatrix}, \mathbf{G} = \begin{pmatrix} \rho \\ \rho u \\ \rho v \end{pmatrix} v + \begin{pmatrix} 0 \\ 0 \\ p \end{pmatrix}. \quad (2)$$

In AUSM, these two terms are separately split at a cell surface. The van Leer-type flux splitting process is applied separately to these two terms (Liou 1996).

We achieve third-order spatial accuracy with the Monotone Upstream-Centered Schemes for Conservation Laws (MUSCL) approach (?). To satisfy the TVD (Total Variation Diminishing) condition using MUSCL, we introduce a limiting function. The code was checked for various test problems, such as one-dimensional and two-dimensional shock tube problems, collision of strong shocks, reflection of shocks at a wall, and propagation of 2-D blast waves. See details in Wada & Norman (2001). We use a Cartesian grid with $128^2 - 2048^2$ zones.

2.1.2 CIP

The Cubic-polynomial Interpolation or Cubic Interpolated Propagation (CIP) method, developed by Yabe et al. (Yabe & Aoki 1991), is a kind of semi-Lagrangian method, in which the hyperbolic equation $\partial \mathbf{f} / \partial t + (\mathbf{u} \cdot \Delta) \mathbf{f} = \mathbf{g}$, where e.g. $\mathbf{f} \equiv (\rho, \mathbf{u})$ and $\mathbf{g} \equiv (-\rho \Delta \cdot \mathbf{u}, -\Delta p / \rho)$, is split into advection and non-advection phases. The former is advanced by using a profile interpolated with a cubic polynomial, and the profile is determined from the time evolution of the quantity \mathbf{f} and the spatial derivative $\Delta \mathbf{f}$. The CIP method is a stable and less diffusive scheme for compressible and incompressible flows with sharp boundaries, and it has been applied to various problems in the field of computational fluid dynamics and astrophysics (e.g., Kudoh, Matsumoto & Shibata 1998 for formation of astrophysical jets). One remarkable feature of this code is that discontinuity is well resolved with relatively small numbers of grid points. The code used here has first-order accuracy in space and time. The number of grid zones used here is the same as that which runs with AUSM.

2.1.3 SPH

We use the Smoothed Particle Hydrodynamics (SPH) code presented by Koda & Wada (2002), which basically uses Benz’s formulation (Benz 1990), using the spline kernel by

Monaghan & Lattanzio (1985) with the modification for its gradient (Thomas & Couchman 1992). The correction term for viscosity is taken into account to avoid large entropy generation in pure shear flows (Balsara 1995). The SPH smoothing length h varies in space and time, keeping the number of particles within the radius of $2h$ at an almost constant of 32 according to the method of Hernquist & Katz (1989). The leapfrog integrator is adopted to update positions and velocities.

In order to represent an initial uniform-density gas disc, we randomly distribute 10^5 gas particles in a 2-D disc with a radius of 3 kpc. The gas particles follow pure circular rotation that balances the centrifugal force.

2.2 Basic equations and Boundary conditions

We solved the following equations numerically in two-dimensions:

$$\frac{\partial \Sigma_g}{\partial t} + \nabla \cdot (\Sigma_g \mathbf{v}) = 0, \quad (3)$$

$$\frac{\partial \mathbf{v}}{\partial t} + (\mathbf{v} \cdot \nabla) \mathbf{v} + \frac{\nabla p}{\Sigma_g} = -\nabla \Phi_{\text{ext}}, \quad (4)$$

where, Σ_g, p, \mathbf{v} are surface density, pressure, and velocity of the gas. Φ_{ext} is a fix external potential. We assume the isothermal equation of state, and gas temperature is 10^4 K, unless otherwise mentioned.

In AUSM and CIP simulations, the boundary conditions are set as follows. In ghost zones at boundaries, the physical values remain at their initial values during the calculations. From test runs, we found that these boundary conditions are much better than other boundary conditions, such as ‘outflow’ boundaries, which cause strong unphysical reflection of waves at the boundaries. Even though this boundary condition does not seem to affect the gas dynamics in the computational box, we put the boundaries far enough from the region where we study the stability of the spiral shocks to avoid unexpected numerical artifacts. The size of the computational box is typically $8 \text{ kpc} \times 8 \text{ kpc}$ (model A, B, and D, see below) or $32 \text{ kpc} \times 32 \text{ kpc}$ (model C). In SPH, we use a free boundary. The simulations are performed in a rotating frame of a fixed pattern speed of the non-axisymmetric potential. We assume initially uniform surface density ($7M_{\odot} \text{ pc}^{-2}$),

2.3 Potential models

We solve two-dimensional gas dynamics in a time-independent, non-axisymmetric external potential. Four different potential models are used; three spiral potentials (model A, B, and C) and one bar potential (model D). One of the spiral models (model C) is assumed a large scale disk (initial radius is 16 kpc), and others and the bar model are for inner galactic disks (initial radii are 4 kpc). Rotation curves derived from the axisymmetric potentials of model A, B, and D, are shown in Fig. 1, and model C in Fig. 2. The four models are defined as below:

$$\text{model A} : \Phi_{\text{ext}} \equiv \Phi_0(R) + \Phi_1(R, \phi), \quad (5)$$

$$\text{model B} : \Phi_{\text{ext}} \equiv \Phi_0(R) + \Phi_2(R) + \Phi_3(R, \phi), \quad (6)$$

$$\text{model C} : \Phi_{\text{ext}} \equiv \Phi_0(R) + \Phi_2(R) + \Phi_3(R, \phi), \quad (7)$$

$$\text{model D} : \Phi_{\text{ext}} \equiv \Phi_0(R) + \Phi_4(R) + \Phi_1(R, \phi), \quad (8)$$

Table 1. Parameters for the four potential models. Units of the core radii are kpc, and km s^{-1} for the velocity v_a , v_b , and v_c .

model	a	b	c	v_a	v_b	v_c
A	1.4	–	–	220	–	–
B	0.2	1.7	–	150	103	–
C	1.3	6.8	–	220	250	–
D	1.4	–	0.01	220	–	311

where the axisymmetric components Φ_0 , Φ_2 , and Φ_4 are defined as

$$\Phi_0(R) \equiv av_a^2(27/4)^{1/2}(R^2 + a^2)^{-1/2}, \quad (9)$$

$$\Phi_2(R) \equiv bv_b^2(27/4)^{1/2}(R^2 + b^2)^{-1/2}, \quad (10)$$

$$\Phi_4(R) \equiv cv_c^2(27/4)^{1/2}(R^2 + c^2)^{-1/2}, \quad (11)$$

and the constants a, b, c, v_a, v_b and v_c in the four models are summarized in Table 1. The non-axisymmetric components (i.e. spiral and bar potentials), Φ_1 and Φ_3 are given by

$$\Phi_1(R, \phi) \equiv \varepsilon_0 \frac{aR^2\Phi_0}{(R^2 + a^2)^{3/2}} \cos[2\phi + 2\cot i \cdot \ln(R/R_0)] \quad (12)$$

$$\Phi_3(R, \phi) \equiv \varepsilon_0 \frac{bR^2\Phi_2}{(R^2 + b^2)^{3/2}} \cos[2\phi + 2\cot i \cdot \ln(R/R_0)] \quad (13)$$

where i is the pitch angle of the spiral potential (see Fig. 12), and R_0 is an arbitrary constant ($R_0 = 0.9$ kpc is used for all models). A constant ε_0 represents maximum strength of the non-axisymmetric potential. For the bar potential model D, $i = \pi/2$ is assumed with Φ_1 .

Model D is chosen in order to see stability of spiral shocks formed by a different mechanism, i.e. resonance-driven spiral shocks. We add a point mass at the galactic centre (Φ_4), which resembles, for example, a supermassive black hole. In model D, the ‘black hole’ mass is assumed to be 1% of the total dynamical mass. This causes a ‘nuclear’ inner Lindblad resonance (nILR), and it is known that trailing spiral shocks are formed around the nILR (Fukuda, Wada, & Habe 1998). This characteristic resonant-driven structure also appears around the outer ILR (Athanassoula 1992; Piner et al. 1995). Using two-dimensional SPH simulations, Fukuda, Habe, & Wada (2000) revealed that the trailing spirals can be gravitationally unstable, and claimed that this process is important in fuelling the gas to the galactic centre. Therefore, stability of such trailing spirals in the galactic nuclear region in cases in which the gas is not self-gravitating is worth studying. We can also study the generality of the stability/instability of the spiral shocks.

3 NUMERICAL RESULTS

In Fig. 3, we show typical numerical results obtained by the three different numerical schemes, i.e. SPH, AUSM, and CIP, explained in section 2.1. ‘Wiggle’ instabilities of the spiral shock, namely ripples of the shock fronts and less dense fin-like structure are clearly seen in all the results. The global morphology of the spirals in all results is quite similar. Comparing Fig. 3(a) with 3(c), one may find that the instability is less prominent in the result by CIP. This is because the CIP code used here is less accurate (i.e. first-order scheme)

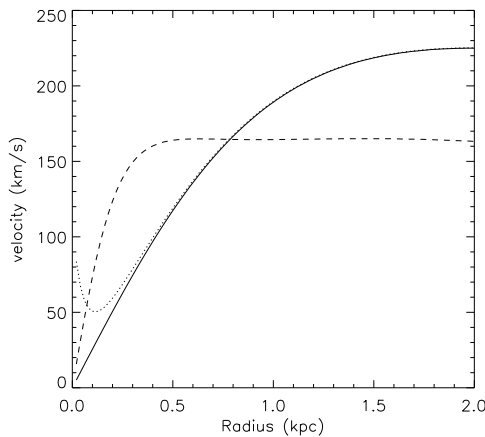


Figure 1. Rotation curves adopted in the numerical simulations. Solid line (model A): nearly rigid rotation models, dashed line: nearly flat rotation curve (model B), and dotted line (model D): the bar model with a central massive black hole.

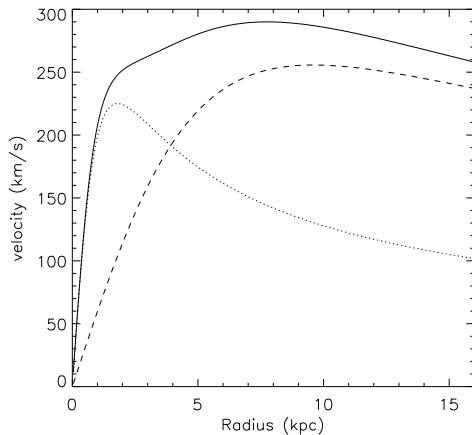


Figure 2. The rotation curve of model C. Solid line: $\Phi_0 + \Phi_2$, dotted line: Φ_0 , and dashed line Φ_2 .

than AUSM (spatial third-order scheme), and therefore the shock is captured less sharply. Although the SPH result is noisier and seems to already be in a non-linear phase especially in the inner region, comparing to the other two results obtained by the mesh-based codes, wavelengths of the instability are similar between the models. The fin-like structures seen in the inter-arm regions are density waves originating in the wiggle instability of the shock front. This phenomenon will be discussed in detail in a subsequent paper (see also section 5).

For further discussion, we use results with the AUSM scheme. The four panels of Fig. 4 show how the numerical results are affected by the spatial resolution. Although global morphology of the spirals is similar in all results, the wiggle instability of the shock fronts is not clear in the results with 128^2 and 256^2 cells. We need at least 512^2 grid points to resolve the instability in this case. Fig. 4 (d) shows that characteristic scale of the ripples is roughly the width of

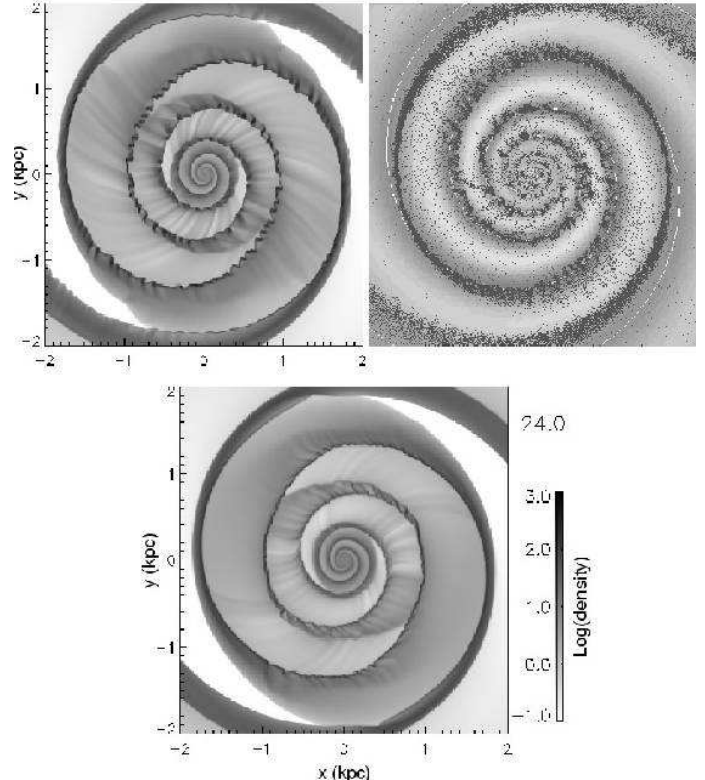


Figure 3. Response of the gas disc to a spiral potential (model A with $i = 10^\circ$, $\varepsilon_0 = 0.1$, $\Omega_p = 26 \text{ km s}^{-1} \text{ kpc}^{-1}$) at $t = 24 \text{ Myr}$. (a) Density distribution given by AUSM with 1024^2 cells. Gray-scale represents log-scaled surface density with a unit of $M_\odot \text{ pc}^{-2}$. (b) SPH with 10^5 particles (roughly there are 4×10^4 particles in this box). Gray-scale represents amplitude of the spiral potential, and the white line is a bottom of the potential. (c) Same as (a), but by CIP.

the shock-compressed layer, which is about 100-200 pc. We can also see that spur-like structures are developed into the inter-arm regions, which are associated with the ripples (see also Fig. 6).

From the azimuthal density profile (Fig. 5), it is clear that reveals sharp shocks where density jump is ~ 100 , and large density fluctuation in the shock compressed layer, which is originated from the clumps seen in Fig. 4, are formed. One may also notice density fluctuation in the inter-arm regions. This can be seen as many ‘crests’ in Fig. 4 (d).

Figure 6 shows time evolution of the spiral shocks in the same model of Fig. 4 (d). The wiggle instability begins in the inner region first, then the outer shocks becomes unstable. At $t = 28 \text{ Myr}$ (d), the instability is in a non-linear stage, and ‘spurs’ are developed in the inter-arm regions towards the other spiral shocks. Typical time-scale of the linear growth of the instability is $\sim 10 \text{ Myr}$ at $R \sim 500 \text{ pc}$ and $\sim 30 \text{ Myr}$ at $R \sim 2 \text{ kpc}$. This is about a half of the orbital time-scale. The spurs are nearly regular spaced, and their intervals seem to be larger in the non-linear phase than in the early phase.

The two panels in Fig. 7 demonstrate that the stability of the shock fronts is sensitive to the pitch angle of the spiral potential (model A). It shows that the shocks are stable for

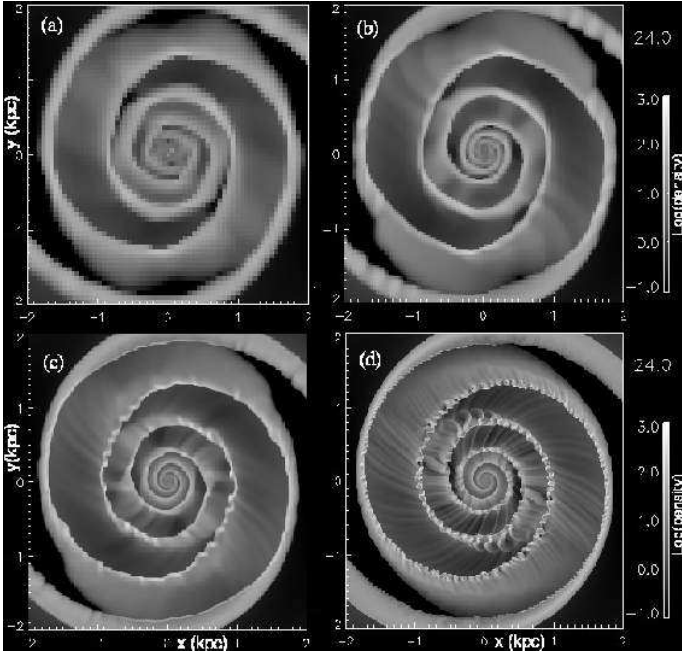


Figure 4. Effect of changing a spatial resolution on the instabilities. The potential model is the same as that in Fig. 3. (a) Density distribution of a central 1/4 region of the computational box with 128^2 cells at $t = 24$ Myr. (b), (c) and (d): Same as (a), but with 256^2 , 512^2 , and 2048^2 , respectively. The parameters used here are the same as those for models in Fig. 3.

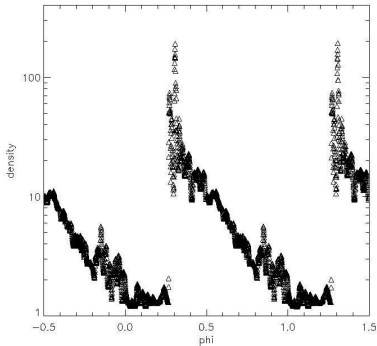


Figure 5. Azimuthal density profile at $R = 1.5$ kpc of Fig. 4 (d). The unit of density is $M_{\odot} \text{ pc}^{-2}$.

$i = 5^\circ$, whereas they are unstable for more loosely wound spirals, i.e. $i = 20^\circ$.

We found that if the rotation curve is flat (model B), the spiral shocks are stable (Fig. 8), provided that the spiral potential is weak (but strong enough to produce the shocks). Note that even if the unperturbed rotation curve is flat, the perturbed potential can cause a radial gradient in the circular velocity on a local scale. This local velocity gradient is essential for the onset of the instability as discussed in section 4 and Appendix.

We found that the wiggle instability of the shocked layer appears not only in the central kpc of galaxies, but also in a larger size disk. Fig. 9 is a snapshot of model C, in which a disk with four times larger size than that in model A and B

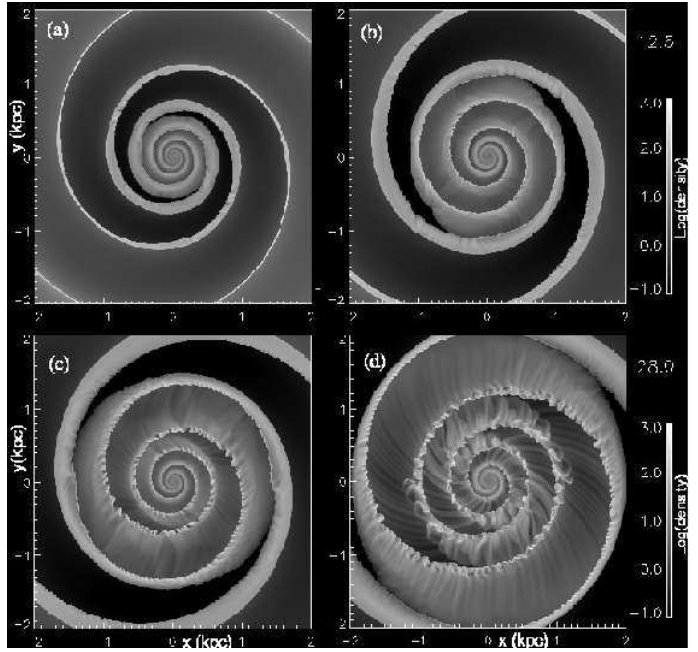


Figure 6. Evolution of the instability in the same model shown in Fig. 4 (d). Four snapshots are at (a) $t = 7.5$ Myr, (b) 12.5 Myr, (c) 17.5 Myr, and (d) 28 Myr.

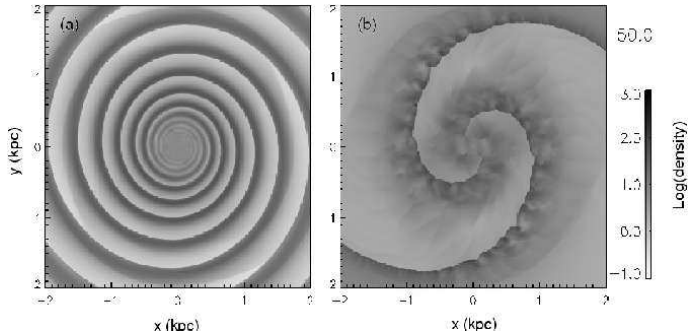


Figure 7. Response of the gas disc to a spiral potential (model A with $i = 5^\circ$ and $i = 20^\circ$). $\varepsilon_0 = 0.1$, $\Omega_p = 26 \text{ km s}^{-1} \text{ kpc}^{-1}$ and $T_g = 10^5 \text{ K}$ at 50 Myr. 1024^2 cells are used in both models.

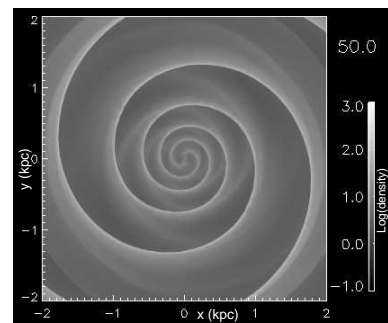


Figure 8. Same as Fig. 7, but for the case that the rotation curve is nearly flat (model B) with $\varepsilon_0 = 0.03$.

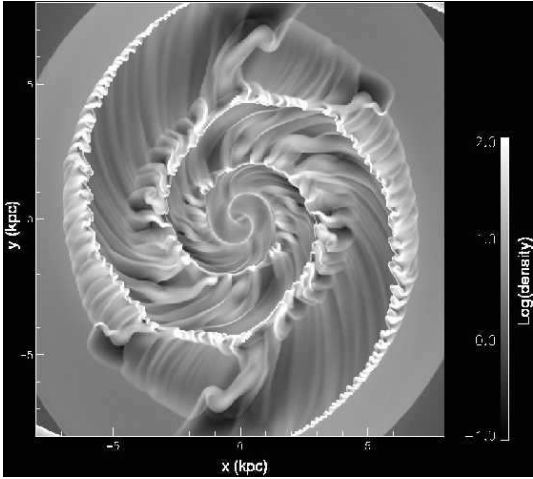


Figure 9. Density distribution in a spiral potential (model C) with $i = 15^\circ$ at $t = 10^8$ yr. 2048^2 cells are used.

is used. The instability and spur-structure in the inter-arm regions are similar between the model A and C, suggesting that the wiggle instability can occur on any scales.

Finally, we examine whether the instability seen in the previous section is a phenomenon peculiar to the spiral potential. Fig. 10 is the density and velocity field near the nuclear Lindblad resonance caused by a central mass concentration, such as a supermassive black hole, in a weak bar potential (model D). In this case, off-set straight shocks are formed outside the nuclear spiral shocks. We found that the shocks are unstable, and they wiggle as seen in the snapshot at $t = 70$ Myr. One may also notice the wavelets in the post-shock regions.

4 DISCUSSION

The results shown in section 3 strongly suggest that the ‘wiggle instability’ of the shocked layers followed by formation of clumps and spurs is not caused by numerical artifacts, but it has a physical origin. We suspect that they originate in the Kelvin-Helmholtz (K-H) instability. As the velocity fields in Fig. 10 and 11 show, there is a strong velocity shear behind the shock. In standing spiral shocks caused in a rotating disk, like galactic shocks or bar-driven shocks, it is most likely that velocity gradient is generated behind the shocks. In general, the K-H instability can develop in a contact surface of two fluid layers with different tangential velocities, even if the velocity difference is small, provided that there is no surface tension. However, in the situation considered here, buoyancy force can suppress the instability, because there is also a density gradient behind the shock under the spiral (or bar) potentials. The Coriolis force could also affect development of the K-H instability (Chandrasekhar 1961). However, for the sake of simplicity, we ignore this kind of effect in the following discussion.

A condition of the K-H *stability* in a sheared layer with a density gradient is characterized using a non-dimensional number, i.e. the Richardson number, J , defined by

$$J \equiv -\frac{g}{\rho} \frac{d\rho/dz}{(du/dz)^2}, \quad (14)$$

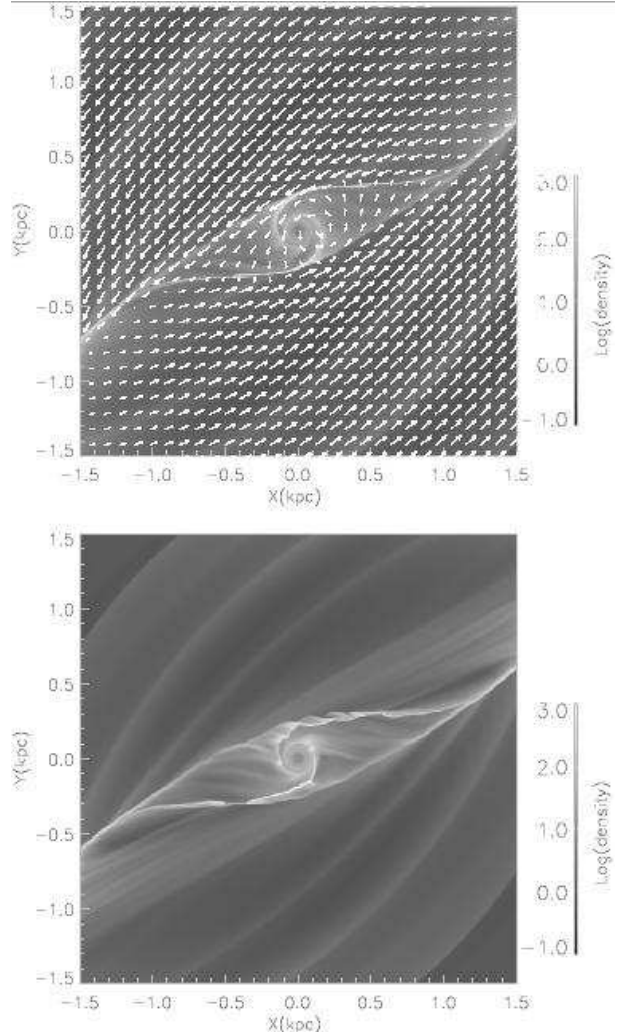


Figure 10. Spiral shocks generated around the nuclear Lindblad resonance. (model D with $\varepsilon_0 = 0.1$, $\Omega_p = 30 \text{ km s}^{-1} \text{ kpc}^{-1}$) at $t = 60$ (upper panel) and 70 Myr (lower panel). Gray-scale is the log-scaled density, and vectors represent a velocity field.

where g is gravitational acceleration, which is normal to the shock front (z -direction), and u is shear velocity. J measures the ratio of the buoyancy force to the inertia, and a *necessary condition* for the K-H *stable* is that $J > 1/4$ (e.g., Chandrasekhar 1961). Here we give a rough estimate of J behind the shock. Figure 12 shows flows passing a spiral shock schematically. The K-H instability could be originated in the velocity shear (Δu) between position B and C, i.e. $v'' > v'$ and v . Equation (14) is then $J \approx 2gd/\Delta u^2$ for the shocked layer with a width of $2d$. Then using

$$g \approx \frac{\partial \Phi_{\text{na}}}{R \partial \eta} \approx \frac{\varepsilon v_\phi^2}{R \sin i}, \quad (15)$$

where Φ_{na} is a non-axisymmetric component of the potential (e.g. Φ_1 or Φ_3 in section 2.3), ε represents a fraction of the non-axisymmetric part to the axisymmetric potential, and v_ϕ is circular velocity, and

$$\Delta u \approx (v'' - v) \cos i \approx v_\phi \left(1 - \frac{1}{M^2}\right) \cos i, \quad (16)$$

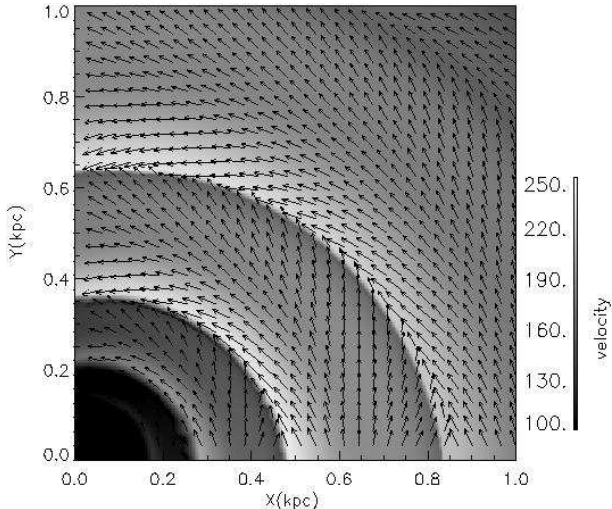


Figure 11. Velocity distribution in the early phase of the evolution for model A with $i = 10^\circ$, $\varepsilon_0 = 0.1$. Gray-scale represents amplitude of the velocity.

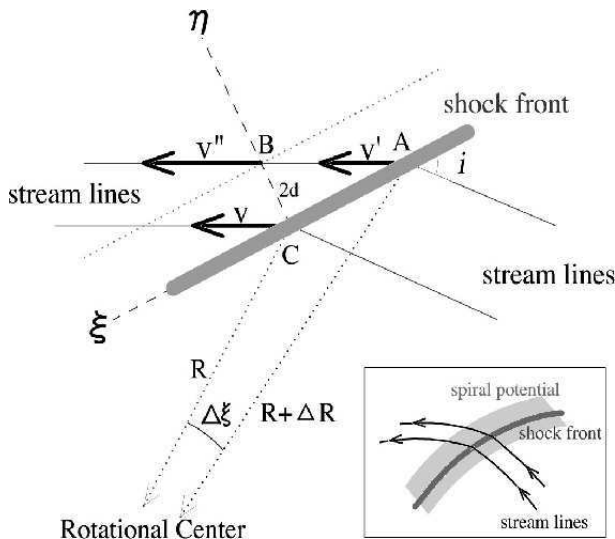


Figure 12. Spiral shock and streamlines, for which we assumed that the curvature can be negligible, and therefore the spiral shocks are modeled as oblique shocks. For $\Delta R \ll R$, the spiral shock can be approximated as an oblique shock. A streamline is changed its direction at point A with velocity v' , and it is accelerated toward the other shock. At point B, its velocity is v'' . A velocity gradient is expected between points B and C. A characteristic scale of the shocked layer is $2d$. (ξ, η) is a orthogonal coordinate along the spiral with the pitch angle, i .

where M is the pre-shock Mach number, the Richardson number can be expressed as a function of the Mach number and the pitch angle:

$$J \approx \frac{2\varepsilon d}{R \sin i (1 - \sin^2 i) (1 - 1/M^2)^2}. \quad (17)$$

This suggests that for a given M , a larger J is obtained for smaller i , and for a larger M , J is smaller. For example, for $\varepsilon = 0.1$, $M = 10$, and $d/R = 0.1$, $J \sim 0.12$ and 0.39 for $i = 10^\circ$ and $i = 3^\circ$, respectively. Although one cannot pre-

dict whether the flow is unstable only from the Richardson criterion, eq. (17) suggests that tightly wound spiral shocks may be relatively stable, comparing to open spirals. This tendency is in fact confirmed by our numerical simulations (e.g. Fig. 7). More detail treatment of the flow and derivation of the Richardson number behind shocks is given in Appendix, where Fig. 13 shows how J depends on the Mach number and the pitch angle, which is qualitatively the same sense of eq. (17).

As the ripples develop in the shock compressed layers, many spur-like structures, or “crests”, which are associated with the clumps, are formed behind the shock, and they extend to the inter-arm regions with a large pitch angle. These structures are morphologically similar to the dust-lanes observed in spiral galaxies. A typical example of this is the central regions of M51 (Scoville et al. 2001, see also Elmegreen 1980). Kim & Ostriker (2002) argued that those spur-like structures are formed as a consequence of magneto-Jeans instability using two-dimensional, local MHD simulations. The wiggle instability we found in the numerical simulations would be an another mechanism to form the spurs, which originates in the K-H instability of the shock-compressed layer. The mechanism of forming spurs is following. The clumps formed by the instability have an internal velocity/angular momentum gradient that causes a phase shift in the orbital motion, and results in deformation of the clumps. Hence, a part of each clump with relatively small angular momenta falls along the spiral shocks, whereas the gases with larger angular momenta try to maintain nearly circular rotation. As a result they move away from the shock toward the other spiral shock. Because of the internal gradient of the angular momentum of a clump formed behind a shock, the clump gas eventually extends to the inter-arm region as it rotates in the galactic potential. One should note that even in a highly nonlinear phase, the global galactic “shocks” are still present, although they are no longer continuous shocks. In subsequent papers, we will discuss the non-linear development of the ripple instability of spiral shocks and the formation mechanism of the spurs. Detail comparison with observations would be also necessary.

In the present simulations, we ignored self-gravity of the ISM. Self-gravity is essential for dynamics and structure of the ISM in galaxies, especially for forming high-density regions and star formation. This is more prominent under the non-axisymmetric external potential (Wada & Koda 2001). As shown in Fig. 5, spiral shocks produce compressed layers where the density is a factor 100 larger than that in the pre-shock region. This is because we assumed isothermal equation of state for the ISM, and the Mach number is ~ 10 . Although this density contrast is comparable to a ratio between a typical density of giant molecular clouds and the average ISM density in a galactic disk, inclusion of self-gravity with realistic cooling processes is necessary to discuss hydrodynamical instabilities in real galaxies. Moreover, it is of interest to study how the gravitational instability of the shocked layer (Balbus & Cowie 1985 and Balbus 1988) relates with the wiggle instability. Even if the post-shock layer is gravitationally stable, self-gravity would trigger collapse of clumps formed by the wiggle instability, and it could lead star formation.

Another interesting phenomenon related with the wiggle instability is interstellar turbulence. In a non-linear

phase, clumps and spurs interact each other, and also collide with other spiral shocks. As a result, irregular motion of the gas is generated, and it could develop turbulent motion of the ISM.

One might think that our findings seem inconsistent with previous studies on spiral shocks. For example, Dwarkadas & Balbus (1996) claimed that the spiral shocks are K-H stable, using a linearized perturbation analysis of the post-shock flow. In their analysis, they numerically integrate a set of linearized perturbed equations assuming a tightly wound spiral (Roberts 1969). They found that the amplitude of the perturbation increases initially for about one-third of a rotation period, and then it decreases by a factor of 20-50 from its maximum value toward a steady state within one rotation period. It should be noted, however, that they assumed a tightly wound spiral in a flat rotation curve ($\kappa = 2\Omega$), which is a preferable condition for the K-H stable as shown in the numerical results and analysis in Appendix. The other point is that one-third of a rotation period would be long enough to form the ripples, clumps and spurs. These sub-structures found in our numerical simulations are not steady, but rather, temporal from a Lagrangian point of view. However, successive formation and destruction of these substructures could keep global, long-lived non-axisymmetric, non-uniform features in the interstellar medium in spiral galaxies.

The instability that we found is not apt to appear in tightly wound spirals with a flat rotation curve. Therefore it is not surprising that the instability has not been found in the many studies in the 60s and 70s on spiral shocks. Yet there have been some pioneering studies on the time-dependent, two-dimensional flow in a spiral potential with various pitch angles. Johns & Nelson (1986) performed such simulations using two distinct codes, i.e. a Eulerian grid code and SPH. Unfortunately their spatial resolution was rather limited ($63^2 \times 2$ polar grid), and as we showed in section 3, this is not fine enough to resolve the instability. However, interestingly, they noticed secondary structures in their spiral arms. The spiral arms in their simulations are not smooth, and local density peaks are seen in the contour maps. They mentioned a possibility of a physical origin of the modulation of the main two-armed response rather than some stochastic or numerical effect, however they did not confirm it. The secondary structure that they found might come from the instability of spiral shocks discussed in this paper.

5 CONCLUSIONS

Using high-resolution numerical simulations, we have found that spiral shocks caused by a galactic spiral potential and by bar-driven resonances can be unstable, in the sense that shocked layers are rippled, and in a non-linear phase they fragment into clumps followed by forming spurs. The instability is most likely caused by the Kelvin-Helmholtz instability in the post-shock layers where density gradient and velocity shear are present under the influence of the gravity of the spiral potential. This instability appears in spiral shocks on small ($R < \text{kpc}$) to large ($\sim 10 \text{ kpc}$) scales, also suggesting that local velocity shear behind the shocks drive it. Spiral shocks tend to be more unstable, if the their pitch angle is larger ($\gtrsim 10^\circ$), and for a higher Mach number

($M \gtrsim 3$). The numerical results are not inconsistent with the discussion using the Richardson criterion (section 4 and Appendix). However, one should be careful that the Richardson criterion itself is just a necessary condition for the K-H stability, and even if $J < 1/4$ the flow could be stable. In this sense, the K-H instability is one possible mechanism of the wiggle instability. We would need careful linear analyses for perturbations in loosely wound spiral shocks for further discussion.

ACKNOWLEDGMENTS

We thank H. Fukuda for his contribution on the CIP code. We are also grateful for N. Scoville, R. Wyse, W. Kim, and Y. Sofue for their comments and suggestions. The anonymous referee also gave us many important suggestions. K. W. was supported by a Grant-in-Aid for Scientific Research (no. 15684003). J. K. was supported by the Japan Society for the Promotion of Science (JSPS) for Young Scientists. A part of numerical works were performed on facilities in Astronomical Data Analysis Center, National Astronomical Observatory of Japan.

APPENDIX: RICHARDSON CRITERION BEHIND A SPIRAL SHOCK

In this Appendix, we stand on a hypothesis, i.e. the wiggle instability found in the numerical experiments is caused by the Kelvin-Helmholtz instability. We give the Richardson number behind the spiral shocks as a function of parameters, such as the Mach number and the pitch angle of the spiral potential. This is useful to evaluate whether the sheared flow can be Kelvin-Helmholtz stable. One should note, however that we simplify the kinematics of the gas in spiral potential, and the Richardson criterion here is not derived from a dispersion relation in a sheared layer caused by open spiral shocks, which may be ultimately given in a future work (see Dwarkadas & Balbus (1996) for linear analysis of tightly wound spiral shocks in a flat rotation curve). Yet a simple ‘toy model’ below would be useful to understand physics behind the numerical results.

We simply assume almost straight streamlines behind the shock and $\Delta R/R \ll 1$ (Fig. 12) as we did in section 4. We also assume that the flow is isothermal, and the asymptotic solutions of the flow in a spiral potential is used to have the velocity and density gradient in the post-shock layer. First we consider only velocity shear which is parallel to the shock as a source of the K-H instability. Effect of the perpendicular velocity, v_ξ , will be considered later.

Under these assumptions, the Richardson number [eq. (14)] can be expressed as

$$J \approx g\sigma d/u_0^2, \quad (18)$$

with the velocity and density differences in a shocked layer, i.e. $u_0^2 \equiv (v_C - v_B)^2/4$ and $\sigma \equiv (\rho_C - \rho_B)/(\rho_C + \rho_B)$ (B and C denote positions shown in Fig. 12), and $2d$ is width of the shock layer.

Width of the shock layer, $2d$, is related to the Mach number M (i.e. $v_\phi/c_s \sin i$, where v_ϕ is the pre-shock velocity

on a rotating frame with a pattern speed Ω_p) and to the pitch angle i as

$$2d = \frac{\Delta R}{\sin i} \tan i / M^2 = \frac{\Delta R}{M^2 \cos i}. \quad (19)$$

As shown in Fig. 12, a flow passing the oblique shock has velocity v' at position A, and is accelerated toward the other spiral shock. As a result, a velocity gradient is generated behind the shock, for example between positions B and C (i.e. $v_{\xi 0}$ and $v''_{\xi 0}$. Subscript “0” denotes unperturbed variables). This velocity gradient, which is normal to the spiral shock, may be a source of the K-H instability. The post-shock velocity transverse to the shock, $v_{\eta 0}$, is $v_{\eta 0}(R) \equiv v_{\phi}(R) \sin i / M^2$, and the post-shock velocity parallel to the shock is $v_{\xi 0}(R) \equiv v_{\phi}(R) \cos i$, and the post-shock velocity at position A is $v'(R) = \sqrt{v_{\xi 0}^2 + v_{\eta 0}^2} = v_{\phi}(R) \sqrt{\cos^2 i + \sin^2 i / M^4}$. The post-shock velocity at position B is

$$v_B \equiv v''_{\xi 0}(R + 2d) = v_{\xi 0}(R + \Delta R) + \Delta v_{\xi}, \quad (20)$$

where $\Delta \xi = \Delta R / (R \sin i)$, and

$$\Delta v_{\xi} \equiv \frac{\partial v_{\xi}(R + \Delta R)}{\partial \xi} \Delta \xi \quad (21)$$

$$= -(R + \Delta R) \frac{v_{\eta 1}}{v_{\eta 0}} \frac{\kappa^2}{2\Omega_c} \Big|_{R + \Delta R} \frac{\tan i}{M^2} \frac{\Delta R}{R \sin i} \quad (22)$$

$$\approx -\frac{v_{\eta 1}}{v_{\eta 0}} \frac{\kappa^2}{2\Omega_c} \frac{\Delta R}{M^2 \cos i}. \quad (23)$$

Here, we use $\partial v_{\xi} / \partial \xi = \partial v_{\xi} / \partial \eta \cdot \Delta \eta / \Delta \xi$, with $\Delta \eta / \Delta \xi = \tan i / M^2$, and the linear solution of flow in a spiral potential (e.g. Spitzer 1978 [equation (13-24)]):

$$\frac{\partial v_{\xi}}{\partial \eta} \sim \frac{\partial v_{\xi 1}}{\partial \eta} \quad (24)$$

$$= -R \frac{v_{\eta 1}}{v_{\eta 0}} \frac{\kappa^2}{2\Omega_c}, \quad (25)$$

where $\Omega_c = v_{\phi}/R + \Omega_p$, $v_{\eta 0} \equiv v_{\phi} \sin i / M^2$, and $v_{\eta 1}/v_{\eta 0}$ is given by

$$v_{\eta 1} \left[-\left(\frac{2v_{\phi}}{R} \right)^2 \left(1 - \frac{c_s^2}{v_{\eta 0}^2} \right) + \kappa^2 \right] = -v_{\eta 0} \frac{\partial^2 \Phi_s}{R^2 \partial \eta^2}, \quad (26)$$

with the epicyclic frequency κ and a spiral potential Φ_s . Using equation (26), equation (23) is rewritten as

$$\Delta v_{\xi} \approx \frac{\frac{\partial^2 \Phi_s}{R^2 \partial \eta^2}}{\left[-\left(\frac{2v_{\phi}(R)}{R} \right)^2 \left(1 - \frac{c_s^2}{v_{\eta 0}^2} \right) + \kappa^2 \right]} \frac{\kappa^2}{2\Omega_c} \frac{\Delta R}{M^2 \cos i} \quad (27)$$

$$= \frac{\frac{\partial^2 \Phi_s}{R^2 \partial \eta^2} \frac{\Delta R}{2\Omega_c M^2 \cos i}}{\left[-2(\alpha + 1)^{-1} \left(1 - M^2 / \sin^2 i \right) + 1 \right]}, \quad (28)$$

where we assume a rotation curve as $v_{\phi} \equiv v_0(R/R_0)^{\alpha}$, therefore $\kappa^2 = 2(\alpha + 1)(v_{\phi}/R)^2$, and $v_{\eta 0} = v_{\phi} \sin i / M^2$ is used. Using $\Phi_s(\eta) \equiv -\varepsilon \Phi_0(R) \sin(2\pi\eta/\pi \sin i)$, in the vicinity of a spiral shock,

$$\frac{\partial^2 \Phi_s}{\partial \eta^2} \Big|_{2d} = \frac{4\varepsilon \Phi_0}{\sin^2 i} \sin \left(\frac{2\eta}{\sin i} \right) \approx \frac{4\varepsilon \Phi_0}{\sin^2 i} \cdot \frac{2\Delta\eta}{\sin i}, \quad (29)$$

where $\Delta\eta = \Delta R / (RM^2 \cos i)$. For a slow pattern speed, i.e. $v_{\phi} \sim R\Omega_c$, from equations (28) and (29) then

$$\frac{\Delta v_{\xi}}{v_{\phi}} = \mu \delta^2, \quad (30)$$

where $\delta \equiv \Delta R / R$, and

$$\mu(M, i, \alpha, \varepsilon) \equiv \frac{4\varepsilon / (M^4 \cos^2 i \cdot \sin^3 i)}{\left[1 - 2(\alpha + 1)^{-1} \left(1 - M^2 / \sin^2 i \right) \right]}. \quad (31)$$

We finally have the velocity variation u_0 in equation (18) using μ and δ :

$$u_0^2 = [(v''_{\xi 0}(R + 2d) - v_{\xi 0}(R)) / 2]^2 \quad (32)$$

$$= \frac{1}{4} \left[\frac{\partial v_{\phi}}{\partial R} \Delta R \cos i + \Delta v_{\xi} \right]^2 \quad (33)$$

$$= \frac{v_{\phi}^2}{4} [\alpha \delta \cos i + \mu \delta^2]^2, \quad (34)$$

where we use $v_{\xi 0}(R + \Delta R) - v_{\xi 0}(R) = [v_{\phi}(R + \Delta R) - v_{\phi}(R)] \cos i$.

The density gradient behind the shock, σ , can be estimated using the mass conservation, namely, $\rho_0 M^2 v'(R + \Delta R) = \rho'' v''(R + 2d)$, which is equivalent to

$$\rho_0 M^2 v_{\phi}(R + \Delta R) (\sin^2 i / M^4 + \cos^2 i) = \rho'' v''_{\xi 0} \left(1 + \frac{\tan^2 i}{M^4} \right)^{1/2}, \quad (35)$$

where $v_{\eta}/v_{\xi} = \tan i / M^2$ is used. Therefore, the dimensionless density change in the layer, σ , is

$$\sigma = \frac{\rho_0 M^2 - \rho''}{\rho_0 M^2 + \rho''} = \frac{1 - \cos i \cdot v_{\phi} / v''_{\xi 0}}{1 + \cos i \cdot v_{\phi} / v''_{\xi 0}} \quad (36)$$

$$= \frac{\alpha \delta \cos i + \mu \delta^2}{2 \cos i + \mu \delta^2 + \alpha \delta \cos i}. \quad (37)$$

The gravitational acceleration, transverse to the shock front, g , is given by

$$g = -\frac{\partial \Phi_s}{R \partial \eta} \quad (38)$$

$$= \frac{v_{\phi}^2}{R} \left[\frac{2\varepsilon}{\sin i} \cos \left(\frac{2\delta}{M^2 \cos i \sin i} \right) \right] \quad (39)$$

Finally, the Richardson number, J , for the flow behind a spiral shock is given combining equations (19), (34), (37), and (39) as

$$J(i, M, \varepsilon, \alpha; \hat{\lambda}) =$$

$$\frac{\frac{4\varepsilon}{\sin i} \cos \left(\frac{2\hat{\lambda}}{M^2 \cos i} \right)}{M^2 \cos i (\alpha \cos i + \hat{\lambda} \sin i) (2 \cos i + \mu \hat{\lambda}^2 \sin^2 i + \alpha \hat{\lambda} \cos i \sin i)}. \quad (40)$$

where $\hat{\lambda}$ is a wavelength normalized by the radius, $\hat{\lambda} \equiv \lambda/R = \delta/\sin i$, and μ is given by equation (31).

In Fig. 13, the Richardson number given by equation (40) is plotted as a function of the Mach number, M , and the pitch angle, i . It shows that J monotonically decreases with M , therefore weaker shock are expected to be more stable. For a given M , a larger J is obtained for smaller i , if $i \lesssim 20^\circ$. This suggests that tightly wound spiral shocks may be relatively stable.

Equation (40) is approximated as $J \approx 4\varepsilon / (i\alpha M^2)$, for $i \ll 1$, $\hat{\lambda} \ll 1$ and $\alpha > 0$. This suggests that spiral shocks in the region of a flat rotation (i.e. $\alpha = 0$) curve are expected to be stable for short wavelengths in a galactic outer region. In fact, one of the numerical results (Fig. 8) shows that shocks in a flat rotation curve is stable. One should note, however, that even if the unperturbed circular velocity is constant, a

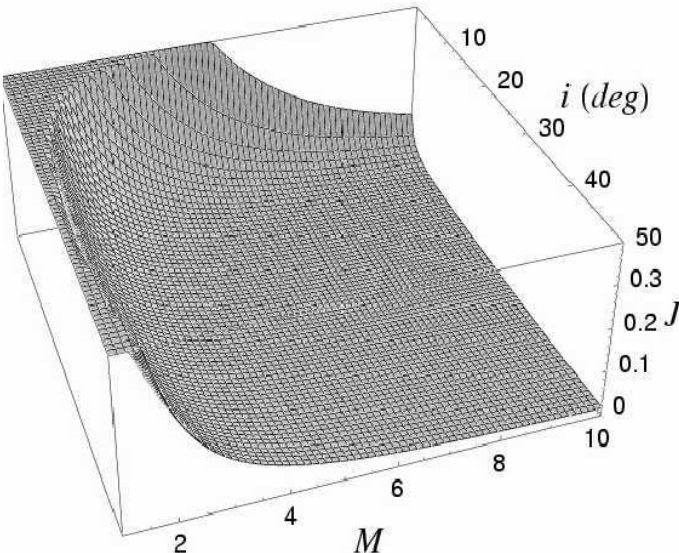


Figure 13. Richardson number, J , behind a spiral shock as a function of Mach number, M , and the pitch angle of the spiral, i , for $\alpha = 1$ (i.e. rigid rotation), $\hat{\lambda} = 0.1$, and strength of the spiral potential, $\varepsilon = 0.1$.

local gradient in circular velocity caused by a spiral potential could destabilize the spiral shocks on a local scale.

In Fig. 14, the critical Richardson numbers are plotted as a function of the Mach numbers and the pitch angles for two different rotation curves. One should note again that $J > 1/4$ does not necessarily mean that the sheared layer is K-H *stable*. This is only a necessary condition for stability as mentioned in section 4.

The curves in Fig. 14 have minima, $M_{\min} \sim 3$ at pitch angles $i_{\min} \sim 30$. The plot shows that the $J = 1/4$ curves decrease with the pitch angle, i , and they increase for $i > i_{\min}$. For $i < i_{\min}$, a flow is less affected by an oblique shock with smaller pitch angles, therefore the velocity gradient behind the shock is smaller, and as a result the shocked layer is expected to be more stable. On the other hand, if the pitch angle is larger than i_{\min} , the width of the sheared layer, $2d$, becomes larger, and again the layer becomes stable. We can also know that weak shocks with $M < M_{\min}$ are expected to be stable for all pitch angles. M_{\min} is larger in the Keplerian rotation curve than for the rigid rotation. This means that spiral shocks generated around a point mass (e.g. an accretion disk in a close-binary) tend to be more stable than those generated in a potential with a constant mass density, for the same pitch angle and the Mach number.

For a given rotation curve, shocks may be more stable in stronger spiral potentials. This is because the K-H instability can be suppressed by buoyancy force, and stronger spiral potentials cause larger gravitational acceleration nearly perpendicular to the shock front [see equation (18)]. One should note however that Mach number of the flow towards the potential minimum is also affected by the strength of the potential, therefore it is not so straightforward to evaluate the effect of the spiral potential on the wiggle instability. If the spiral potential is too weak (e.g. amplitude of the spiral component is less than a few % of the axisymmetric one), shocks do not appear in the flow (e.g. Shu et al. 1973).

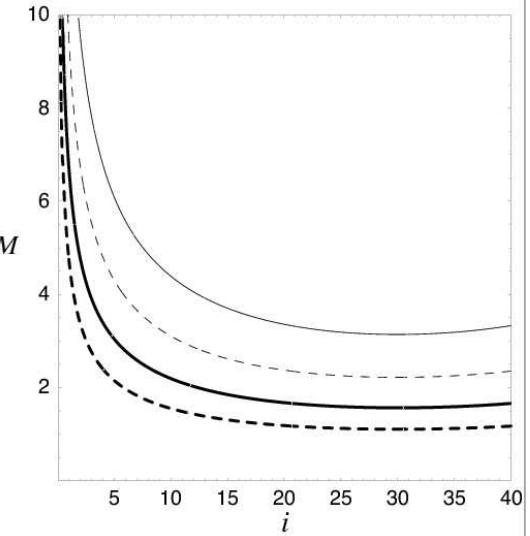


Figure 14. Curves for $J = 1/4$ are plotted as a function of the pitch angle i (degree) and Mach number M , below which the spiral shocks could be Kelvin-Helmholtz stable (i.e. $J > 1/4$, see Fig. 13 and the text). Thick curves are for rigid rotation ($\alpha = 1$), and thin curves are for Keplerian ($\alpha = -1/2$) with $\varepsilon = 0.1$ (solid curves) and 0.05 (dashed curves). $\hat{\lambda} = 0.01$ is assumed.

In above discussion, we neglect the effect of expansion (perpendicular to the shock) velocity, v_ξ . In fact, the flow behind the shock has the expansion velocity, which is approximately

$$\Delta v_\eta \approx (v''_{\xi 0} - v_{\xi 0}) \Delta \eta / \Delta \xi = 2u_0 \tan i / M^2 = \frac{4u_0}{M_0^2 \sin 2i}, \quad (41)$$

where $M_0 \equiv v_\phi / c_s$. If $\Delta v_\eta^2 > u_0^2$, we expect that the shear layer is stable for the K-H instability due to the expansion flow. From eq. (41), it is suggested that the expansion velocity becomes important for spirals with a small pitch angle and/or small Mach number (see also Dwarkadas & Balbus 1996). For example, this can be happen when $M_0 < 2.5$, 3.4 , and 4.8 , for the spirals with $i = 20$, 10 , and 5° , respectively. In other words, for strong shocks with a large pitch angle, the post shock flow is nearly parallel to the shock, and then the expansion velocity on the K-H instability can be negligible. This is consistent with our numerical results.

REFERENCES

- Athanassoula, E. 1992, MNRAS, 259, 345
- Balbus, S. A. 1988, ApJ, 324, 60
- Balbus, S. A. & Cowie, L. L. 1985, ApJ, 297, 61
- Balsara, D.S. 1995, Journal of Computational Physics, 121, 357
- Benz, W. 1990, The Numerical Modeling of Nonlinear Stellar Pulsations, p.269, Kluwer Academic Publishers
- Chandrasekhar, S., 1961, “Hydrodynamic and Hydromagnetic Stability”, Dover, New York, p.481
- Dwarkadas, V. V., Balbus, S. A. 1996, ApJ, 467, 87
- Elmegreen D. M., 1980, ApJ, 242, 528
- Elmegreen B. G., 1994, ApJ, 433, 3

Fumimoto, M. 1968, in IAU sympo. No.29 "Non-stable phenomena in galaxies", The publishing house of the Academy of Sciences of Armenia, Verevan, p. 453

Fukuda H., Habe A., Wada K., 2000, ApJ, 529, 109

Fukuda H., Wada K., Habe A., 1998, MNRAS, 295, 463

Hernquist, L. and Katz, N. 1989, ApJ Suppl., 70, 419

Ishibashi, S. & Yoshii, Y. 1984, PASJ, 36, 41

Johns, T. C., Nelson, A. H. 1986, MNRAS, 220, 165

Kim, W., Ostriker, E. C. 2002, ApJ, 570, 132

Koda, J., Wada, K. 2002, A&Ap, 396, 867

Kudoh T., Matsumoto R., Shibata K., 1998, ApJ, 508, 186

Lin C. C., Shu F. H., 1964, ApJ, 140, 646

Liou, M., Steffen, C., 1993, J.Comp.Phys., 107, 23

Liou, M., 1996, J.Comp.Phys., 129, 364

Lubow, S. H., Cowie, L. L., Balbus, S. A. 1986, ApJ, 309, 496

Mishurov, I. N., Suchkov, A. A. 1975, Ap&Space Sci., 35, 285

Monaghan, J.J. and Lattanzio, J.C. 1985, A&Ap, 149, 135

Nelson A. H., Matsuda T., 1977, MNRAS, 179, 663

Piner B. G., Stone J. M., Teuben P. J., 1995, ApJ, 449, 508

Roberts, W. W. 1969, ApJ, 158, 123

Sawa T., 1977, PASJ, 29, 781

Scoville N. Z., Polletta M., Ewald S., Stolovy S. R., Thompson R., Rieke M., 2001, AJ, 122, 3017

Shu, F. H., Milione, V., Gebel, W., Yuan, C., Goldsmith, D. W., Roberts, W. W. 1972, ApJ, 173, 557

Shu, F. H., Milione, V., Roberts, W. W. 1973, ApJ, 183, 819

Thomas, P.A. and Couchman, H.M.P. 1992, MNRAS, 257, 11

Tomisaka, K. 1987, PASJ, 39, 109

Wada, K., 2001, ApJ 559, L41

Wada, K. & Koda, J. 2001, PASJ, 53, 1163

Wada, K., Norman, C.A., 1999, ApJ, 516, L13

Wada, K., Norman, C.A., 2001, ApJ, 546, 172

Wada, K., Norman, C.A., 2002, ApJ, 566, L21

Wada, K., Gerhardt, M., Norman, C.A., 2002, ApJ, 577, 197

Wada, K., Spaans, M., Kim, S., 2000, ApJ, 540, 797

Woodward, P. R. 1975, ApJ, 195, 61

Yabe, T., Aoki, T. 1991, Comput. Phys. Commun., 66, 219

This paper has been typeset from a TeX/ L^AT_EX file prepared by the author.